



CHORUS

This is the accepted manuscript made available via CHORUS. The article has been published as:

Enhanced doping efficiency of ultrawide band gap semiconductors by metal-semiconductor junction assisted epitaxy

A. Pandey, X. Liu, Z. Deng, W. J. Shin, D. A. Laleyan, K. Mashooq, E. T. Reid, E. Kioupakis, P. Bhattacharya, and Z. Mi

Phys. Rev. Materials **3**, 053401 — Published 9 May 2019

DOI: [10.1103/PhysRevMaterials.3.053401](https://doi.org/10.1103/PhysRevMaterials.3.053401)

**Enhanced Doping Efficiency of Ultrawide Bandgap
Semiconductors by Metal-Semiconductor Junction Assisted
Epitaxy**

**A. Pandey¹, X. Liu^{1,2}, Z. Deng³, W. J. Shin¹, D. A. Laleyan¹, K. Mashooq¹, E. T.
Reid¹, E. Kioupakis³, P. Bhattacharya¹, and Z. Mi^{1,*}**

¹*Department of Electrical Engineering and Computer Science, University of Michigan,*

1301 Beal Avenue, Ann Arbor, Michigan 48109, USA

²*Department of Electrical and Computer Engineering, McGill University*

3480 University Street, Montreal, Quebec H3A 0E9, Canada

³*Department of Materials Science and Engineering, University of Michigan,*

2300 Hayward Street, Ann Arbor, Michigan 48109, USA

*: E-mail: ztmi@umich.edu; Phone: (734) 764-3963

Ultrawide bandgap semiconductors are important for a broad range of electronic and photonic devices, but their practical application has been limited by poor current conduction. Here, we demonstrate that with controlled tuning of the Fermi level by an in-situ metal-semiconductor junction during epitaxy, efficient p-type conduction, that was otherwise impossible, can be achieved for large bandgap aluminum gallium nitride (AlGaN). During epitaxy, the Fermi level is pinned away from the valence band edge, which fundamentally reduces the formation energy for substitutional Mg-dopant incorporation while simultaneously increasing the formation energy for compensating defects. We have demonstrated that Mg-doped Al_{0.9}Ga_{0.1}N can exhibit free hole concentration $\sim 4.5 \times 10^{17} \text{ cm}^{-3}$, with resistivity $< 5 \text{ } \Omega \cdot \text{cm}$, which is nearly three orders of magnitude lower compared to previous reports. Ultraviolet 280 nm light emitting diodes grown using this method exhibited nearly an order of magnitude improvement in external quantum efficiency compared to those grown using conventional molecular beam epitaxy. Such a unique technique can be extended for the epitaxy/synthesis of a broad range of wide bandgap semiconductors to achieve efficient current conduction that was not previously possible.

I. INTRODUCTION

Wide bandgap semiconductors such as GaN, AlN and their alloys have emerged as the materials of choice for high power and high frequency electronic devices [1,2], as well as a broad range of photonic devices including ultraviolet (UV) light emitting diodes (LEDs) [3], lasers [4] and solar blind photodetectors. Critical for the operation and

performance of these devices is a precise control of the doping level in the different layers of the structure. To date, however, it has remained extremely challenging to achieve efficient p-type conduction of AlN and AlGaN with relatively high Al content, which has been identified as one of the major obstacles to realize high performance optoelectronic devices operating in the mid and deep UV spectra. Magnesium (Mg) has been established as the only viable p-type dopant of group III-nitride semiconductors [5]. However, it exhibits very large activation energy (up to 600 meV) in Al-rich AlGaN [6-8], severely limiting the doping efficiency and the realization of large hole concentration at room temperature. Extensive studies have been performed to realize low-resistivity p-type AlGaN, including the use of a high V/III ratio to suppress formation of compensating nitrogen vacancies, superlattices consisting of alternating AlGaN layers, metal modulation epitaxy (MME), Mg δ -doping, indium as a surfactant and polarization-induced doping, but with very limited success [9-31]. For example, the lowest resistivity reported for p-type Al_{0.85}Ga_{0.15}N epilayers [21] to date is well over $10^3 \Omega\cdot\text{cm}$, which is more than three orders of magnitude larger than that of Mg-doped GaN.

To achieve p-type AlGaN with large hole concentration and low resistivity, it is essential to incorporate large densities of Mg-dopant atoms. At very large concentrations ($\sim 10^{19}$ - 10^{20} cm^{-3}), an Mg impurity band is expected to form, which enables hole hopping conduction [32,33]. Moreover, the significantly broadened acceptor energy levels at large Mg-doping concentrations, together with the band tailing effect, also reduces the ionization energy for a fraction of Mg-dopants. In practice, however, it becomes more difficult to incorporate Mg into AlGaN with increasing Al concentration, due to the larger formation enthalpy (lower solubility) for Mg substituting Al in the AlGaN lattice sites,

compared to Ga [6,34]. Theoretical calculations in the Supplementary Materials [35] confirm the difficulty in substitutional Mg incorporation, especially in Al sites. The formation energy for various compensating point defects also depends critically on the position of the Fermi level [5,6]. During conventional epitaxy, with Mg-dopant incorporation, the Fermi level shifts towards the valence band edge, illustrated in Figs. 1(a) and (b), which significantly reduces the formation energy for carbon, oxygen, and nitrogen vacancies [6,9,36,37]. These defects have a strong compensating effect and further degrade the structural, electronic, and optical properties of Mg-doped AlGaN. In addition, the formation energy of N-substitutional and interstitial Mg incorporation decreases drastically with Mg incorporation, and becomes comparable to that of Al(Ga)-substitutional Mg incorporation when the Fermi level is positioned close to the valence band edge, further limiting the doping efficiency and the achievement of large hole concentrations. Evidently, some of the critical issues for achieving efficient p-type conduction of AlGaN can be well addressed, if the Fermi level at the growth front can be tuned away from the valence band during the epitaxy of p-type (Mg-doped) AlGaN.

To overcome these fundamental challenges, we investigate a unique epitaxial growth process – metal-semiconductor junction assisted epitaxy – of ultrawide bandgap AlGaN. Illustrated in Fig. 1(c), the epitaxy of AlGaN is performed in metal (Ga) rich conditions by using plasma-assisted molecular beam epitaxy (MBE). The excess Ga layer leads to the formation of a metal-semiconductor junction during the epitaxy of Mg-doped AlGaN, which pins the Fermi level away from the valence band at the growth front, illustrated in Fig. 1(d). In this unique epitaxy process, the Fermi level position is decoupled from Mg-dopant incorporation, *i.e.*, the surface band bending allows the

formation of a nearly n-type growth front despite p-type dopant incorporation, which is in direct contrast to the fixed Fermi level position near the valence band edge during the conventional epitaxy of Mg-doped AlGaN. As such, the formation energy for substitutional Mg is dramatically reduced, even when very large densities of Mg-dopant atoms are incorporated, which is accompanied by a significant suppression of the formation of compensating defects. Epitaxy of AlGaN under metal-rich conditions was reported previously. However, the role of Fermi-level tuning at the growth front and the resulting effect on the enhanced substitutional incorporation of Mg and suppressed compensating defect formation was not identified [38-41]. [Figure 1\(e\)](#) illustrates the variation of the theoretically calculated substitutional formation energy, for Mg in GaN, AlN, and Al_{0.5}Ga_{0.5}N, with the energy separation between the Fermi level and valence band maximum. These calculations are explained in the next section, and details of the band structure calculations for AlGaN during growth using the two methods is discussed in the Supplementary Materials [35]. By increasing the separation between the Fermi level and valence band, the formation energy is reduced to only ~0.43 eV for metal-semiconductor junction assisted epitaxy of AlGaN, which is ~1.6 eV lower than that during growth using conventional epitaxy. This powerful method simply relies on the spontaneous formation of a metal-semiconductor junction at the growth interface by excess Ga and does not involve any modification of the system under use. In this growth regime, the Al composition of AlGaN can be controllably varied by tuning the Al material flux while keeping the nitrogen flow rate constant. This is because the bond strength of Al-N is much stronger compared to that of Ga-N [42,43] and, as a consequence, Al-N will preferably form while any excess Ga will accumulate on the

surface to form the metal-semiconductor junction during epitaxy. Utilizing this technique, we have demonstrated that Mg incorporation in AlGaN can be enhanced by nearly one order of magnitude compared to the conventional growth process: Mg concentration $\sim 2 \times 10^{20} \text{ cm}^{-3}$ was measured in $\text{Al}_{0.75}\text{Ga}_{0.25}\text{N}$ for a moderate Mg flux of $\sim 7 \times 10^{-8}$ Torr. A significant reduction of carbon impurity incorporation was also confirmed through detailed secondary ion mass spectrometry (SIMS) measurements. Significantly, a free hole concentration of $\sim 4.5 \times 10^{17} \text{ cm}^{-3}$ was measured for $\text{Al}_{0.9}\text{Ga}_{0.1}\text{N}$, with resistivity values $< 5 \text{ } \Omega \cdot \text{cm}$, which is nearly three orders of magnitude lower compared to previous reports [21]. Ultraviolet 280 nm light-emitting diodes fabricated using the two methods demonstrated significant improvements in the device characteristics and efficiency for the samples grown by metal-semiconductor junction assisted epitaxy, as compared to the sample grown using the conventional growth mode.

II. METHODOLOGY

A. Theoretical Calculations

Density functional theory calculations were performed with HSE06 hybrid functional [44] and projected augmented wave method [45, 46], as implemented in Vienna *Ab initio* Simulation Package (VASP) [47]. GW-compatible pseudopotentials were used, where Mg 3s, Al 3s3p, Ga 4s4p, and N 2p states were treated as valence electrons. The fraction of non-local Hartree-Fock exchange in the hybrid functional is 0.30 for GaN and $\text{Al}_{0.5}\text{Ga}_{0.5}\text{N}$, and 0.33 for AlN, giving their band gap values of 3.51 eV, 4.65 eV, and 6.20 eV respectively, in close agreement with the experiments [48-50]. Defect calculations were performed for GaN, $\text{Al}_{0.5}\text{Ga}_{0.5}\text{N}$ and AlN using 96-atom orthorhombic supercells

[51] with $2 \times 2 \times 2$ Gamma-center k-point grid and a plane wave energy cut-off of 500 eV. Special quasi-random supercell (SQS) of $\text{Al}_{0.5}\text{Ga}_{0.5}\text{N}$ were generated by Alloy Theoretic Automated Toolkit (ATAT) [52]. All structures were relaxed until the force on ions is less than $0.02 \text{ eV } \text{\AA}^{-1}$, with spin-polarization included for un-paired electrons. Corrections to the charged defects were employed, based on Freysoldt scheme [53], which eliminates the electrostatic interactions between image charges in the supercell approach.

B. Molecular Beam Epitaxial Growth

The samples used in this work were grown on $\sim 1 \text{ }\mu\text{m}$ AlN-on-sapphire substrates from DOWA Holdings Co. Ltd. using a plasma-assisted Veeco Gen 930 MBE system. The Mg-doped AlGaN epilayers were grown at a temperature $\sim 700 \text{ }^\circ\text{C}$ (thermocouple reading), and the Al flux was varied for samples with different Al compositions. The nitrogen flow was 0.4 standard cubic centimeter per minute, with a forward plasma power of 350 W. The reflection high energy electron diffraction (RHEED) pattern was closely monitored during epitaxy to determine the growth condition, which was achieved by varying the Ga flux. A relatively dim and streaky RHEED pattern indicated that the growth was under metal-rich conditions, whereas a brighter pattern with segmented streaks suggests the growth is in slightly N-rich conditions.

The growth was initiated with an undoped AlN buffer layer, followed by $\sim 30 \text{ nm}$ undoped AlGaN, before the growth of the Mg-doped AlGaN layer. The thickness of the AlGaN layers for Hall measurement was approximately 430 nm. For the samples grown for Hall measurements, the growth is terminated with a $\sim 2 \text{ nm}$ p-GaN capping layer, which was subsequently etched in the fabrication process for Hall measurements.

For the samples on which SIMS was performed, the grown structure consisted of several AlGa_N layers grown with different Mg fluxes, with undoped layers in between. The Mg flux used in the different layers of the samples on which SIMS was performed was measured at different temperatures before every growth, using a beam flux monitor (BFM) equipped in the MBE system.

The LED heterostructure consists of a 250 nm thick Si-doped Al_{0.7}Ga_{0.3}N layer, multiple Al_{0.45}Ga_{0.55}N/Al_{0.7}Ga_{0.3}N quantum wells, 60 nm thick Mg-doped AlGa_N layer, and 3 nm p-GaN contact layer. The first 30 nm Mg-doped AlGa_N layer was graded from an Al composition ~70% to 50% to make use of polarization induced doping to maximize hole injection into the active region [54], followed by a 30 nm thick Mg-doped Al_{0.5}Ga_{0.5}N. An AlGa_N electron blocking layer was also incorporated to reduce electron overflow. The device active region was calibrated for emission at ~280 nm.

C. Characterization

The composition of AlGa_N epilayers was derived from Vegard's law based on X-ray diffraction measurements, which were performed using a Rigaku SmartLab X-ray diffractometer. The sample surface was examined by scanning electron microscopy (SEM) using a Hitachi SU8000 cold field emission SEM. Atomic force microscopy (AFM) scans of the sample surface was taken by a Bruker Dimension Icon AFM, operated under tapping mode in air, to determine the surface roughness. SIMS was performed by EAG Laboratories to derive Mg-dopant atom concentration and C-impurity atom concentration. Photoluminescence spectroscopy measurements were performed at room temperature using a 193 nm ArF excimer laser as the excitation source.

D. Device Fabrication

For the Schottky diodes fabricated on Mg-doped AlGaIn layers, a metal stack consisting of Ni (20 nm)/Al (100 nm)/Au (20 nm) was first deposited for the ohmic contact and annealed at 500 °C for 5 minutes in the presence of air. The p-GaN layer that was outside of the Ni/Al/Au metal contact was removed using a low-power plasma etch with BCl₃/Cl₂ chemistry. Then, a 200 nm thick Ti layer was deposited for the Schottky contact. The area of the diodes was 500 μm × 500 μm. To fabricate the samples for Hall measurements, metal contacts consisting of Ni (20 nm)/Al (100 nm)/Au (20 nm) were defined using photolithography and deposited by e-beam evaporation, followed by annealing at 500 °C for 5 minutes in the presence of air. The thin p-GaN contact layer was subsequently isolated and removed. The UV LED fabrication process involves the use of standard photolithography, dry etching and contact metallization techniques. The device mesa has an area 50 μm × 50 μm. A Ti (40 nm)/Al (120 nm)/Ni (40 nm)/Au (50 nm) metal stack was deposited on n-AlGaIn and annealed at 750 °C for 30 seconds in nitrogen ambient to form the n-metal contact. A Ni (20 nm)/Al (100 nm)/Au (20 nm) metal stack was deposited on p-AlGaIn and annealed at 500 °C for 5 minutes in air to form p-metal contact.

III. RESULTS AND DISCUSSION

A. Effect on Mg Incorporation

We have first studied the extraordinary effect of a metal-semiconductor junction on Mg-dopant incorporation during the epitaxy of AlGa_N with Al composition ~75%. Sample A was grown under Ga-rich conditions, using metal-semiconductor junction assisted epitaxy, to ensure complete coverage of the substrate surface with metallic Ga during growth, while Sample B was grown under nearly stoichiometric conditions using the conventional growth mode but with otherwise identical conditions, *e.g.*, the same growth rate and same Mg fluxes, for corresponding layers. Subsequently, Mg concentrations were obtained using SIMS measurements. Details about the Ga coverage during epitaxy are presented in the Supplementary Materials [35]. [Figure 2\(a\)](#) shows the Mg atom concentration profile for the two samples, wherein the different Mg-doped AlGa_N layers are separated by undoped layers. It is seen that, with the use of metal-semiconductor junction assisted epitaxy, Mg concentrations are significantly higher than those grown using the conventional growth method. Variations of the Mg incorporation vs. Mg flux, measured as beam equivalent pressure (BEP) for the two samples are further plotted in [Fig. 2\(b\)](#). For both samples, Mg concentration increases with Mg BEP. However, the Mg atom density is over an order of magnitude higher for Sample A grown with metal-semiconductor junction assisted epitaxy, as compared to Sample B using the conventional process. The maximum Mg incorporation achieved for Sample A was $\sim 2 \times 10^{20}$ Mg atoms cm^{-3} , without showing any sign of saturation. The significantly enhanced Mg incorporation is attributed to the reduced formation energy for Al(Ga)-substitutional Mg incorporation [5,6,37] when the Fermi level is pinned away from the valence band edge by utilizing the metal-semiconductor junction at the growth front. We would also like to point out that the C-impurity concentration was significantly reduced compared to

MOCVD. For the sample grown using metal-semiconductor junction assisted epitaxy, the carbon concentration is limited by the measurement background of SIMS ($\sim 1 \times 10^{16} \text{ cm}^{-3}$). For comparison, carbon concentrations $\sim 5 \times 10^{16} \text{ cm}^{-3}$ to $2 \times 10^{18} \text{ cm}^{-3}$ have been commonly measured in Al-rich AlGa_{0.25}N grown by MOCVD [55]. The pinning of Fermi level at the growth front through metal-semiconductor junction assisted epitaxy also leads to a significant decrease in the formation of point defects, which explains the observation that undoped (Al)Ga_{0.25}N layers grown under Ga-rich conditions showed approximately three orders of magnitude higher resistivity compared to films grown under conventional conditions [6,38].

B. Photoluminescence Characteristics

We further studied the photoluminescence properties of the sample grown using metal-semiconductor junction assisted epitaxy. A typical photoluminescence spectrum for a Mg-doped Al_{0.75}Ga_{0.25}N sample is shown in Fig. 2(c). A strong peak near the band-edge at $\sim 255 \text{ nm}$ (4.86 eV) was measured, accompanied with the Mg-acceptor related transition at $\sim 298 \text{ nm}$ (4.16 eV). It has been previously reported that this emission originates from a donor-acceptor pair transition in Mg-doped AlGa_{0.25}N epilayers [39]. The broad linewidth of the Mg-acceptor related transition and its partial overlap with the band-edge luminescence emission indicates a very large spread of the Mg-acceptor energy levels, extending nearly to the valence band edge of AlGa_{0.25}N. Evidently, the significantly enhanced Mg dopant incorporation can not only lead to the formation of an impurity band for hole hopping conduction [31-33], but more importantly, results in substantially reduced activation energies for a portion of Mg-dopants, thereby enabling

the presence of large hole carrier concentrations at room temperature in AlGaN, that were not possible otherwise [56].

C. Low-Resistivity p-type AlGaN with High Al Content

By employing the metal-semiconductor junction assisted epitaxy, we have also grown a series of Mg-doped samples with Al compositions varying from ~75% up to ~90%. Atomic force microscopy measurements indicated a smooth surface with roughness below 1 nm for all the samples. Hall measurements were performed on the samples, using the van der Pauw method, to determine the hole concentration, hole mobility and resistivity of the AlGaN layers for temperatures ranging from room temperature to 500 °C. The room temperature hole concentration is observed to monotonically decrease with increasing Al content, illustrated in Fig. 3(a). Figure 3(b) shows variations of hole mobility with the Al composition. The decrease in hole concentration and mobility with increasing Al composition can be explained by a reduction in Mg incorporation for alloys with a higher Al mole fraction due to the lower solubility of Mg and the increased formation enthalpy for Al-substitutional Mg [5,57]. Even for the incorporated Mg atoms, the increase in the activation energy of the Mg-acceptor with increasing Al content further shrinks the free hole concentration. This reduction in Mg concentration with increasing Al composition has been further verified through SIMS measurements of AlGaN samples grown with different alloy compositions, but with the same Mg BEP, shown in the Supplementary Materials [35]. These factors result in an increase in the resistivity for Mg-doped AlGaN layers with increased Al composition, shown in Fig. 3(c). However even for Al_{0.9}Ga_{0.1}N, the measured resistivity remains below 5 Ω·cm. The

resistivity values of some previously reported Mg-doped AlGa_N layers [9-31] are plotted vs. Al compositions in Fig. 3(d), along with the resistivity of the AlGa_N layers obtained in this work. It is seen that the resistivities of Mg-doped AlGa_N grown using metal-semiconductor junction assisted epitaxy is nearly one to three orders of magnitude lower compared to previously reported results.

D. Hole Conduction Mechanism

We have further measured variations of the hole concentration vs. temperature for Mg-doped AlGa_N samples with different Al compositions, illustrated in [Figure 4\(a\)](#). A low activation energy (~10-20 meV) at temperatures less than 600 K is seen in these samples, which is characteristic of hole hopping conduction in the impurity band [13,14] and can also be partly explained that a portion of the Mg dopants have significantly reduced activation energy, evidenced by the photoluminescence spectrum shown in [Fig. 2\(c\)](#) [31,58]. At higher temperatures, more Mg-dopants get activated, contributing to holes in the valence band. This leads to a sharp increase in hole concentration at elevated temperatures (>650 K), which is characterized by a large activation energy (~300-400 meV). Such activation energy values, however, are somewhat lower than those theoretically expected [6] for AlGa_N alloys with Al compositions ~75-90%. This can be explained by the presence of band-tailing effects and the significantly broadened acceptor energy level distribution, which effectively reduces the activation energy for a portion of Mg-acceptors. The measured hole mobility, shown in [Fig. 4\(b\)](#), has a monotonically decreasing trend with increasing temperature, as expected due to an increase in phonon scattering. The resistivity, shown in [Fig. 4\(c\)](#), is first observed to increase with temperature between 300 K and ~650 K due to the decrease in hole mobility and relatively small change in hole concentration. At higher temperatures, when the Mg acceptors get thermally activated, the dramatic rise in hole concentration results in the observed decrease in resistivity.

E. UV LED Characteristics

The significantly reduced resistivity of Mg-doped AlGa_N, enabled by the unique metal-semiconductor junction assisted epitaxy, is crucial to improve the efficiency of optoelectronic devices operating in the mid and deep UV wavelengths. We have fabricated and characterized AlGa_N UV LEDs, emitting at ~280 nm, grown using this unique approach, and compared the device characteristics with identical LEDs grown using conventional epitaxy. A typical electroluminescence spectrum is shown in Fig. 5(a), with a narrow linewidth ~11 nm. The current-voltage characteristic is shown in Fig. 5(b), which exhibits a turn-on voltage of ~7 V for the LED grown using metal-semiconductor junction assisted epitaxy, while we see a turn-on voltage ~9 V for the conventional epitaxy sample. The higher turn-on voltage is likely a result of the ineffective Mg-doping when using conventional epitaxy. The external quantum efficiency (EQE) was further measured directly on wafer, without any packaging, substrate removal, or cooling. Shown in Fig. 5(c), a maximum on-wafer EQE of ~4.3% was measured at room temperature, which is significantly better than the LED device grown using the conventional epitaxy process, which exhibits a maximum EQE of ~0.6%. This device performance is also better than other previously reported AlGa_N UV LEDs grown by MBE around this wavelength [38,39,59,60]. The improved device-characteristics seen in the samples grown using metal-semiconductor junction assisted epitaxy highlights the significance of efficient p-type conduction on device performance. It is also worth noting that the measured EQE can be significantly increased through proper packaging of devices to increase the light extraction efficiency, and by employing more comprehensive techniques to capture all the emitted light, such as the use of an integrating sphere.

IV. CONCLUSION

In summary, we have demonstrated that, by tuning the surface Fermi level using metal-semiconductor junction assisted epitaxy, efficient p-type conduction can be achieved for Al-rich AlGa_{0.75}N that was not previously possible. The presence of a metal-semiconductor interface at the growth front pins the Fermi level away from the valence band edge, which can significantly enhance Al(Ga)-substitutional Mg-dopant incorporation and further reduces the formation of compensating point defects, as demonstrated in this work, both theoretically and experimentally. It should also be noted that the presence of surface states, which are strongly affected by growth conditions as has been previously described for both polar [61] and non-polar [62] surfaces, may further play a role in pinning the Fermi level away from the valence band, although the surface state density structure at the elevated temperatures required for crystal growth has remained unknown. As such, large concentrations of Mg-acceptors can be incorporated in Al-rich AlGa_{0.75}N, which enables the formation of a Mg impurity band. Al-rich AlGa_{0.75}N epilayers, with resistivity values below 1 Ω·cm for Al_{0.75}Ga_{0.25}N and ~4 Ω·cm for Al_{0.9}Ga_{0.1}N have been measured, which are essentially required for achieving high efficiency mid and deep UV optoelectronic devices. Deep UV LEDs grown using this method showed a great improvement in external quantum efficiency, and lower turn-on voltage, as compared to devices grown using conventional epitaxy. Such a unique technique can be further extended for the epitaxy/synthesis of a broad range of semiconductor nanostructures and heterostructures to achieve controlled dopant incorporation and to fundamentally improve their structural, electronic, and optical properties.

ACKNOWLEDGEMENTS

Experimental work was performed in the Lurie Nanofabrication Facility at the University of Michigan, Ann Arbor. The authors would like to thank Binh Tinh Tran for his assistance in developing the fabrication procedure for the UV LED. The authors acknowledge financial support from the University of Michigan College of Engineering. This research used resources of the National Energy Research Scientific Computing Center, a DOE Office of Science User Facility supported by the Office of Science of the U.S. Department of Energy under Contract No. DE-AC02-05CH11231.

REFERENCES

- [1] A. Raman, S. Dasgupta, S. Rajan, J. S. Speck, and U. K. Mishra, *Jpn. J. Appl. Phys.* **47**, 3359 (2008).
- [2] R. J. Kaplar, A. A. Allerman, A. M. Armstrong, M. H. Crawford, J. R. Dickerson, A. J. Fischer, A. G. Baca, and E. A. Douglas, *ECS J. Solid State Sci. Technol.* **6**, Q3061 (2017).
- [3] S. Inoue, N. Tamari, and M. Taniguchi, *Appl. Phys. Lett.* **110**, 141106 (2017).
- [4] K. H. Li, X. Liu, Q. Wang, S. Zhao, and Z. Mi, *Nature Nanotechnology* **10**, 140 (2015).
- [5] C. Stampfl and C. G. Van de Walle, *Phys. Rev. B* **65**, 155212 (2002).
- [6] C. Stampfl and C. G. Van de Walle, *Appl. Phys. Lett.* **72**, 459 (1998).
- [7] U. Kaufmann, P. Schlotter, H. Obloh, K. Köhler, and M. Maier, *Physical Review B* **62**, 10867 (2000).
- [8] M. L. Nakarmi, N. Nepal, C. Ugolini, T. M. Altahtamouni, J. Y. Lin, and H. X. Jiang, *Appl. Phys. Lett.* **89**, 152120 (2006).
- [9] Y. Taniyasu, M. Kasu, and T. Makimoto, *Nature* **441**, 325 (2006).
- [10] Y. Chen, H. Wu, E. Han, G. Yue, Z. Chen, Z. Wu, G. Wang, and H. Jiang, *Appl. Phys. Lett.* **106**, 162102 (2015).
- [11] K. Ebata, J. Nishinaka, Y. Taniyasu, and K. Kumakura, *Jpn. J. Appl. Phys.* **57**, 04FH09 (2018).
- [12] T. C. Zheng, W. Lin, R. Liu, D. J. Cai, J. C. Li, S. P. Li, and J. Y. Kang, *Scientific Reports* **6**, 21897 (2016).
- [13] T. Kinoshita, T. Obata, H. Yanagi, and S. Inoue, *Appl. Phys. Lett.* **102**, 012105 (2013).
- [14] P. Kozodoy, M. Hansen, S. P. DenBaars, and U. K. Mishra, *Appl. Phys. Lett.* **74**, 3681 (1999).
- [15] M. L. Nakarmi, K. H. Kim, M. Khizar, Z. Y. Fan, J. Y. Lin, and H. X. Jiang, *Appl. Phys. Lett.* **86**, 092108 (2005).
- [16] M. L. Nakarmi, K. H. Kim, J. Li, J. Y. Lin, and H. X. Jiang, *Appl. Phys. Lett.* **82**, 3041 (2003).
- [17] K. Kumakura and N. Kobayashi, *Jpn. J. Appl. Phys.* **38**, L1012 (1999).
- [18] A. A. Allerman, M. H. Crawford, M. A. Miller, and S. R. Lee, *Journal of Crystal Growth* **312**, 756 (2010).
- [19] M. Suzuki, J. Nishio, M. Onomura, and C. Hongo, *Journal of Crystal Growth* **189–190**, 511 (1998).
- [20] H. Yu, E. Ulker, and E. Ozbay, *Journal of Crystal Growth* **289**, 419 (2006).
- [21] A. Kakanakova-Georgieva, D. Nilsson, M. Stattin, U. Forsberg, Å. Haglund, A. Larsson, and E. Janzén, *Physica Status Solidi (RRL) – Rapid Research Letters* **4**, 311 (2010).
- [22] Z. Li, J. Li, H. Jiang, Y. Han, Y. Xia, Y. Huang, J. Yin, and S. Hu, *Advances in Condensed Matter Physics* **2014**, 5 (2014).
- [23] M. Z. Kauser, A. Osinsky, A. M. Dabiran, and P. P. Chow, *Appl. Phys. Lett.* **85**, 5275 (2004).
- [24] J. K. Kim, E. L. Waldron, Y.-L. Li, T. Gessmann, E. F. Schubert, H. W. Jang, and J.-L. Lee, *Appl. Phys. Lett.* **84**, 3310 (2004).

- [25] E. L. Waldron, J. W. Graff, and E. F. Schubert, *Appl. Phys. Lett.* **79**, 2737 (2001).
- [26] W. Bao-Zhu, W. Xiao-Liang, H. Guo-Xin, R. Jun-Xue, W. Xin-Hua, G. Lun-Chun, X. Hong-Ling, Li Jian-Ping, Z. Yi-Ping, L. Jin-Min, and W. Zhan-Guo, *Chinese Phys. Lett.* **23**, 2187 (2006).
- [27] I. D. Goepfert, E. F. Schubert, A. Osinsky, P. E. Norris, and N. N. Faleev, *Journal of Applied Physics* **88**, 2030 (2000).
- [28] S. A. Nikishin, M. Holtz, and H. Temkin, *Japanese Journal of Applied Physics* **44**, 7221 (2005).
- [29] Z. Xiaowei, L. Peixian, X. Shengrui, and H. Yue, *J. Semicond.* **30**, 043002 (2009).
- [30] K. B. Nam, M. L. Nakarmi, J. Li, J. Y. Lin, and H. X. Jiang, *Appl. Phys. Lett.* **83**, 878 (2003).
- [31] X. Liu, A. Pandey, D. A. Laleyan, K. Mashooq, E. T. Reid, W. J. Shin, and Z. Mi, *Semicond. Sci. Technol.* **33**, 085005 (2018).
- [32] B. Gunning, J. Lowder, M. Moseley, and W. Alan Doolittle, *Appl. Phys. Lett.* **101**, 082106 (2012).
- [33] M. S. Brandt, N. M. Johnson, R. J. Molnar, R. Singh, and T. D. Moustakas, *Appl. Phys. Lett.* **64**, 2264 (1994).
- [34] M. L. Nakarmi, N. Nepal, J. Y. Lin, and H. X. Jiang, *Appl. Phys. Lett.* **94**, 091903 (2009).
- [35] See Supplemental Material at [insert hyperlink](#) for first principle calculations of formation energy for substitutional Mg incorporation, details about Ga surface coverage during growth, capacitance-voltage characteristics of Schottky diodes and variation of Mg incorporation for different AlGaIn compositions.
- [36] C. G. Van de Walle, C. Stampfl, and J. Neugebauer, *Journal of Crystal Growth* **189–190**, 505 (1998).
- [37] C. G. Van de Walle and J. Neugebauer, *Journal of Applied Physics* **95**, 3851 (2004).
- [38] T. D. Moustakas and A. Bhattacharyya, *Physica Status Solidi C* **9**, 580 (2012).
- [39] Y. H. Liang and E. Towe, *Journal of Applied Physics* **123**, 095303 (2018).
- [40] A. Bhattacharyya, W. Li, J. Cabalu, T. D. Moustakas, D. J. Smith, and R. L. Hervig, *Appl. Phys. Lett.* **85**, 4956 (2004).
- [41] Y.-H. Liang and E. Towe, *Applied Physics Reviews* **5**, 011107 (2018).
- [42] E. Iliopoulos and T. D. Moustakas, *Appl. Phys. Lett.* **81**, 295 (2002).
- [43] W. E. Hoke, A. Torabi, J. J. Mosca, and T. D. Kennedy, *Journal of Vacuum Science & Technology B: Microelectronics and Nanometer Structures Processing, Measurement, and Phenomena* **25**, 978 (2007).
- [44] J. Heyd, G. E. Scuseria, and M. Ernzerhof, *J. Chem. Phys.* **118**, 8207 (2003).
- [45] P. E. Blöchl, *Phys. Rev. B* **50**, 17953 (1994).
- [46] G. Kresse and D. Joubert, *Phys. Rev. B* **59**, 1758 (1999).
- [47] G. Kresse and J. Furthmüller, *Phys. Rev. B* **54**, 11169 (1996).
- [48] R. Dingle, D. D. Sell, S. E. Stokowski, and M. Ilegems, *Phys. Rev. B* **4**, 1211 (1971).
- [49] W. M. Yim, E. J. Stofko, P. J. Zanzucchi, J. I. Pankove, M. Ettenberg, and S. L. Gilbert, *Journal of Applied Physics* **44**, 292 (1973).
- [50] F. Yun, M. A. Reshchikov, L. He, T. King, H. Morkoç, S. W. Novak, and L. Wei, *Journal of Applied Physics* **92**, 4837 (2002).
- [51] C. G. Van de Walle, S. Limpijumng, and J. Neugebauer, *Phys. Rev. B* **63**, 245205

(2001).

- [52] A. van de Walle, P. Tiwary, M. de Jong, D. L. Olmsted, M. Asta, A. Dick, D. Shin, Y. Wang, L.-Q. Chen, and Z.-K. Liu, *Calphad* **42**, 13 (2013).
- [53] C. Freysoldt, J. Neugebauer, and C. G. V. de Walle, *Physica Status Solidi (B)* **248**, 1067 (2011).
- [54] J. Simon, V. Protasenko, C. Lian, H. Xing, and D. Jena, *Science* **327**, 60 (2010).
- [55] A. Tian, J. Liu, M. Ikeda, S. Zhang, Z. Li, M. Feng, K. Zhou, D. Li, L. Zhang, P. Wen, F. Zhang, and H. Yang, *Appl. Phys. Express* **8**, 051001 (2015).
- [56] N. H. Tran, B. H. Le, S. Zhao, and Z. Mi, *Appl. Phys. Lett.* **110**, 032102 (2017).
- [57] T. Zheng, W. Lin, D. Cai, W. Yang, W. Jiang, H. Chen, J. Li, S. Li, and J. Kang, *Nanoscale Res Lett* **9**, 40 (2014).
- [58] R. J. Molnar, T. Lei, and T. D. Moustakas, *Appl. Phys. Lett.* **62**, 72 (1993).
- [59] Y. Zhang, Z. Jamal-Eddine, F. Akyol, S. Bajaj, J. M. Johnson, G. Calderon, A. A. Allerman, M. W. Moseley, A. M. Armstrong, J. Hwang, and S. Rajan, *Appl. Phys. Lett.* **112**, 071107 (2018).
- [60] Y. Liao, C. Thomidis, C. Kao, and T. D. Moustakas, *Applied Physics Letters* **98**, 081110 (2011).
- [61] C. G. Van de Walle and D. Segev, *Journal of Applied Physics* **101**, 081704 (2007).
- [62] J. E. Northrup and J. Neugebauer, *Phys. Rev. B* **53**, R10477 (1996).

FIGURE CAPTIONS

FIG. 1. (a) Schematic of conventional epitaxy. (b) Energy band diagram of the Mg-doped AlGaN layer during conventional epitaxy. (c), Schematic of metal-semiconductor junction assisted epitaxy, with the presence of a liquid Ga layer on the surface during epitaxy. (d) Energy band diagram at the growth front of Mg-doped AlGaN during metal-semiconductor junction assisted epitaxy, showing the pinning of the surface Fermi level away from the valence band edge. (e) Calculated formation energy for Mg substitution in GaN, AlN, and $\text{Al}_{0.5}\text{Ga}_{0.5}\text{N}$ as a function of the separation between the Fermi level and the valence band with substitutional Mg formation energies for the different growth processes indicated by their respective arrows.

FIG. 2. (a), Mg atom concentration versus depth obtained from SIMS measurements on Mg-doped $\text{Al}_{0.75}\text{Ga}_{0.25}\text{N}$ grown using metal-semiconductor junction assisted epitaxy and conventional epitaxy. (b) Mg concentration versus the Mg flux for Mg-doped $\text{Al}_{0.75}\text{Ga}_{0.25}\text{N}$ grown using metal-semiconductor junction assisted epitaxy and conventional epitaxy. (c), Photoluminescence spectra of a Mg-doped $\text{Al}_{0.75}\text{Ga}_{0.25}\text{N}$ sample grown using metal-semiconductor junction assisted epitaxy with band-edge peak and Mg-acceptor peak shown with arrows.

FIG. 3. Room-temperature Hall measurement data for Mg-doped AlGaN epilayers plotted against Al composition, showing (a) free hole concentration, (b) hole mobility, (c)

resistivity and (d), resistivities of Mg-doped AlGa_N layers obtained from literature and this work.

FIG. 4. Temperature dependent Hall measurement of Mg-doped AlGa_N epilayers grown by metal-semiconductor junction assisted, with Al content between 75% and 90%, for (a) hole concentration, (b) hole mobility and (c) resistivity plotted against the inverse of temperature.

FIG. 5. (a) Electroluminescence spectrum for an UV LED grown using metal-semiconductor junction assisted epitaxy. (b) I-V characteristics for LEDs grown using metal-semiconductor junction assisted epitaxy and conventional epitaxy. (c) EQE versus current density for these devices.

FIGURES

FIG. 1.

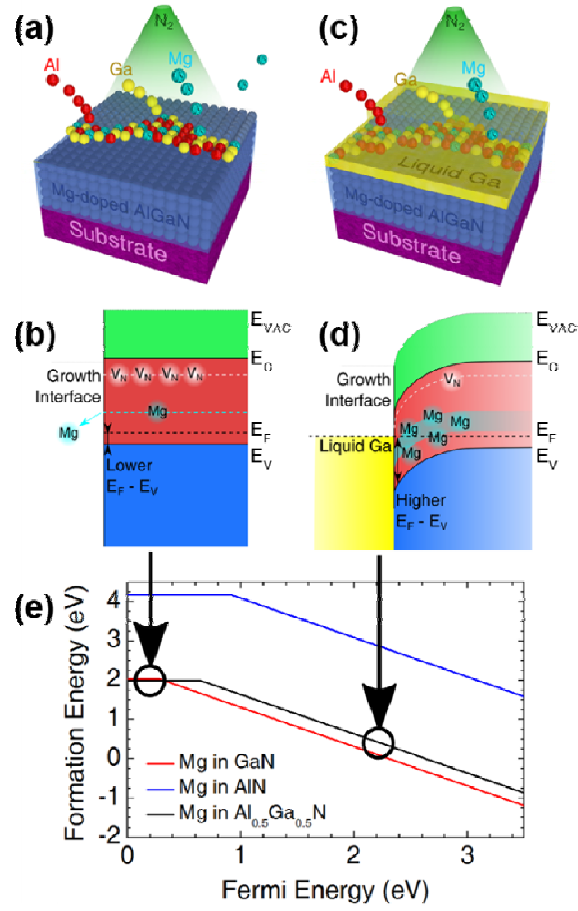


FIG. 2.

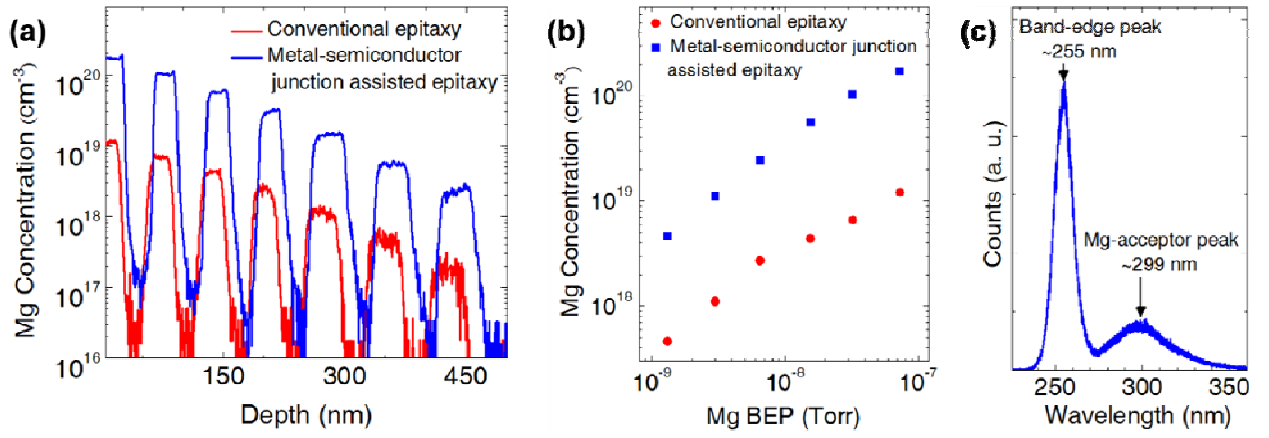


FIG. 3.

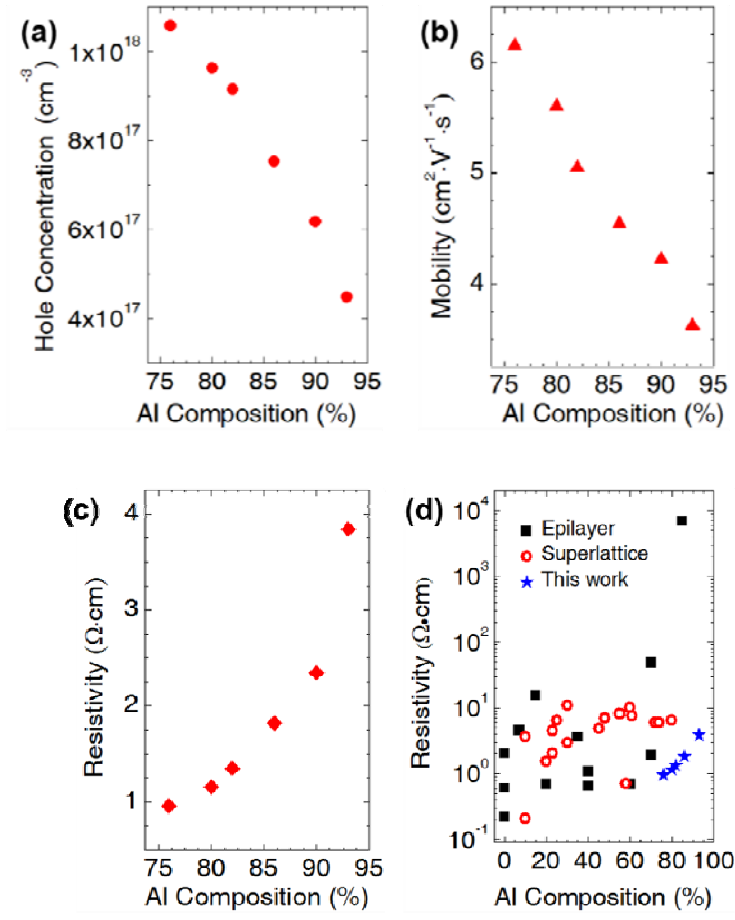


FIG. 4.

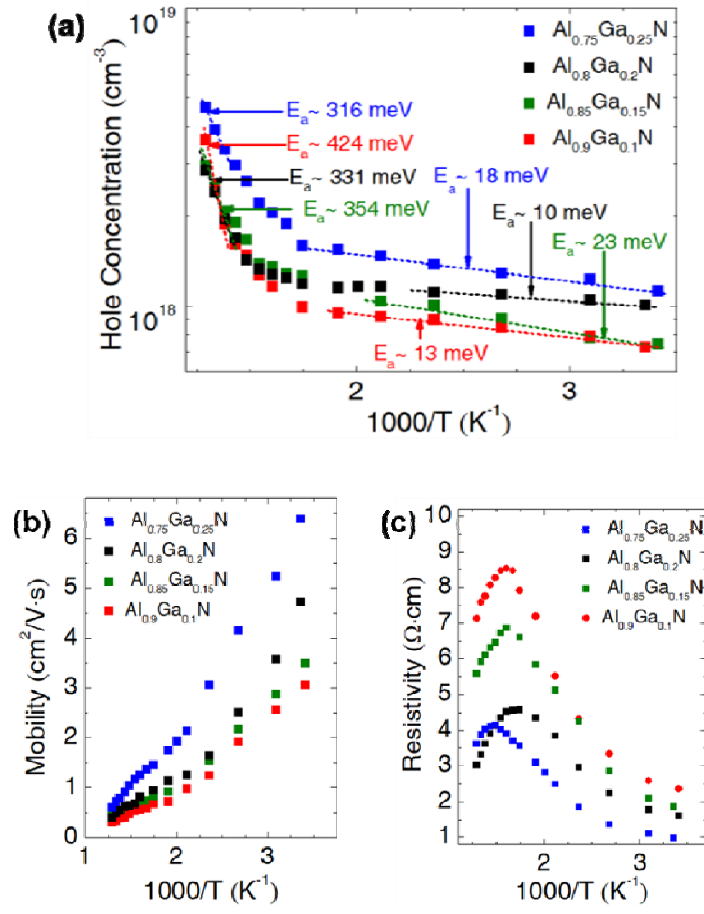


FIG. 5.

